Highlights

Fine-scale phytoplankton community transitions in the oligotrophic ocean: a Mediterranean Sea case study

Laurina Oms, Monique Messié, Jean-Christophe Poggiale, Gérald Grégori, Andrea Doglioli

- Oceanographic cruises show quick phytoplankton changes across small areas and periods;

- A simple model was used to investigate these fine-scale community transitions;

- The interplay of bottom-up and top-down controls explains the observations;

- Fine-scale dynamics drive spatio-temporal phytoplankton transitions.

Fine-scale phytoplankton community transitions in the oligotrophic ocean: a Mediterranean Sea case study

Laurina Oms[a], Monique Messié[b], Jean-Christophe Poggiale[a], Gérald Grégori[a], Andrea Doglioli[a]

[a]*Aix Marseille Univ., Toulon University CNRS, IRD MIO UM 110
Marseille, 13288, France*
[b]*Monterey Bay Aquarium Research Institute, , Moss Landing, CA, USA*

Abstract

In the ocean the vast phytoplankton diversity, shaped by intricate water dynamics, remains poorly understood. *In situ* studies reveal fine-scale dynamics affecting phytoplankton distribution, leading to abrupt shifts in abundances and biomasses referred here as Phytoplankton Community Transitions (PCTs). Using a simple NP2Z model, our study proposes a theoretical framework to explain PCTs observed during an oceanographic cruise in the Mediterranean Sea. We consider both a homogeneous and a variable environment, respectively corresponding to the waters on both sides of a front and to the frontal area itself. We evidence that PCTs between one community of smaller phytoplankton and one community of bigger phytoplankton are controlled by nutrient supply, but not directly: nutrient supply affects all compartments of the model and creates PCTs by combining bottom-up and top-down controls. This mechanism is observed for both constant (i.e., in the water masses) and pulsed nutrient supply (i.e., in the front). These results are consistent with *in situ* observations of biomass proportion on each side of a front. This theoretical framework helps to better understand *in situ* observations in oceanic regions characterized by fine-scale dynamics and oligotrophic conditions.

Keywords: trophic interactions, fine-scales, phytoplankton ecology, NPZ modelling, cytometry

1. Introduction

The ocean displays dynamic movements that transport water masses from one region to another across various spatio-temporal scales. Marine phytoplankton cells are particularly affected by ocean movements because of their limited self-propelled movement ability. Understanding phytoplankton distribution is crucial for their pivotal role in the biological sequestration of carbon with transfer to the higher trophic network, and thus in controlling the ecological structure of the ocean (Frederiksen et al., 2006). The phytoplankton's diversity is vast, with a wide array of shapes, sizes, and ecological traits, among others (Dutkiewicz et al., 2020). In nutrient-poor and low-biomass oligotrophic conditions, acknowledging fine-scale dynamics (1–100 km, days–months) can boost primary production by 10 to 30% (Lévy et al., 2001). Oligotrophic regions span 60% of the ocean surface (Longhurst, 1998), representing the planet's largest cohesive ecosystems (Moutin et al., 2017), and are set to expand with future warming (Polovina et al., 2008). As a consequence, it is essential to understand phytoplankton dynamics at fine-scales in oligotrophic regions in order to predict future changes in carbon sequestration and ecosystems.

Fine-scales fronts are created by the encounter between water masses of distinct origins with different characteristics such as temperature and salinity (McWilliams, 2021). 3D frontal dynamics impact biogeochemistry by influencing transport, both by acting as horizontal barriers and by creating vertical fluxes (Mahadevan and Archer, 2000). In particular, upward currents bring nutrients, supporting more phytoplankton diversity and biomass (Lévy et al., 2015; Clayton et al., 2017). Several studies examined how fine-scale fronts affect biology (Hitchcock et al., 1993; Yoder et al., 1987; Mahadevan, 2016; Lévy et al., 2018; Mangolte, 2022). The influence of frontal areas extends beyond the front itself as it shapes the surrounding environment. The ocean landscape resembles a mosaic of patches and boundaries, with fronts defined as the delineating boundaries between contrasting water patches, marking regions of transition or separation (Acha et al., 2015). Despite its importance, the role of fine-scale fronts on biology is still relatively unknown because the small size of the front, their ephemeral characteristics and uncertain dynamics make them challenging to observe *in situ* (Lévy et al., 2012).

Only oceanographic cruises specially designed for fine-scale studies allow

plankton patches and their boundaries to be identified and tracked. The OS-CAHR cruise in the Ligurian Sea combined high-resolution measurements of both physical and biological variables, revealing the influence of physical dynamics on the spatial distribution of phytoplankton through an eddy structure (Marrec et al., 2018). The SHEBEX cruise in the Balearic Sea showed that the Lagrangian properties of the flow have important biological consequences from phytoplankton to high ecological levels (Hernández-Carrasco et al., 2020). The PROTEVSMED-SWOT cruise performed in the south-western Mediterranean Sea showed constrasted abundances of the phytoplankton communities in two water masses on either side of a front: picophytoplankton (microphytoplankton) were more abundant in the southern (northern) side of the front (Tzortzis et al., 2021). These shifts of phytoplankton size across a frontal area also exist in others region (e.g. in the California Current Ecosystem Sea, Taylor et al., 2012). All these studies underscore the intimate connection between fine-scale dynamics and abrupt phytoplankton abundance and biomass shifts over relatively limited distances and time periods that are referred to here as "Phytoplankton Community Transitions (PCTs)". According to Lévy et al. (2018), three sets of fine-scale processes can elucidate observed PCTs: i) the passive process linked to horizontal transport; ii) the active process linked to vertical transport; and iii) the reactive process linked to biotic interactions, such as zooplankton grazing. The first process creates so-called fluid dynamical niches (d'Ovidio et al., 2010). The second one influences nutrient transport, which affects the bottom-up controls on phytoplankton (Clayton et al., 2014) and, consequently, the trophic chain structure (Poggiale et al., 2013). The third process was shown to be another important component in the structuring of phytoplankton communities by several modelling studies (McCauley and Briand, 1979; Adjou et al., 2012; Zheng et al., 2022).

In this work we focus on fine-scale frontal dynamics and associated contrasts in phytoplankton abundances and biomass, exploring two hypotheses: i) fronts influence nutrient fluxes through physical processes (bottom-up control), involving both active and passive processes, and ii) fronts affect biotic interactions, including zooplankton grazing (top-down control), involving the reactive process. We build our scientific questioning on the *in situ* observed contrasted abundances by Tzortzis et al. (2021), linked to contrasted growth rates (Tzortzis et al., 2023). But a comprehensive explanation of the processes associated to the observations is still lacking.

The aim of this article is to explain the processes leading to the observed PCTs using a simple modelling framework. Several modelling studies have explored issues of coupling between physics and biology, ranging from models with very simple formulations (e.g. Grover, 1990) to models of great complexity (e.g. Aumont et al., 2015). NPZ (Nutrient, Phytoplankton, Zooplankton) models are a common tool in oceanography for their ability to have simple formulations, few parameters and various applications (Franks, 2002). In this study we used a NP2Z model adapted to oligotrophic regions and applied in two scenarios: one with constant forcing simulating homogeneous water masses, and another with pulsed forcing simulating the variable environment of a frontal area.

The article is structured into three sections. The Materials and Methods introduce the PROTEVSMED-SWOT cruise, *in situ* biomass calculations, and the NP2Z model. The Results section displays findings from both *in situ* data and model simulations, with the latter presented in two parts: constant forcing and pulsed forcing. The Discussion section proposes a theoretical framework for the observed PCTs.

2. Material and methods

2.1. In situ cruise and biomass calculation

During the PROTEVSMED-SWOT campaign (May 2018, south of the Balearic Islands (Dumas, 2018)), we defined a sampling strategy to cross a frontal zone separating different water masses. We conducted high-resolution physical and biological measurements. We obtained surface data from a CTD sensor mounted on a towed vehicle and a flow cytometer installed on the surface water intake. Employing an adaptive Lagrangian sampling strategy, we identified two water masses near a fine-scale frontal area with contrasting abundances of nine phytoplankton clusters defined by flow cytometry (Tzortzis et al., 2021). These two water masses were sampled along a designated ship route, with a focus on capturing the phytoplankton diel cycle. Both water masses were continuously sampled along transects, defining the region as the "hippodrome" between May 11 and May 13, 2018. The two water masses are named here according to their respective location with the front: the northern and southern water masses.

Observed contrasts was compared here with model results. To allow an accurate comparison with the numerical model output and previous studies, phytoplankton abundances need to be expressed in terms of biomass. Cell carbon content can be estimated from cell biovolume (corresponding to the 3D space occupied by a cell), enabling measured abundances ($cell\,m^{-3}$) to be converted into biomasses ($mmolC\,m^{-3}$) (Menden-Deuer and Lessard, 2000). The biovolume (BioV [$\mu m^3/cell$]) was calculated by converting optical measurements by flow cytometry according to Eq. 1a (Foladori et al., 2008; Marrec et al., 2018; Tzortzis et al., 2023). The carbon content (Q_c [$mmolC\,cell^{-1}$]) was calculated according to Eq. 1b (Menden-Deuer and Lessard, 2000). The biomass (BioM [$mmolC\,m^{-3}$]) was then calculated for each measurement by multiplying phytoplankton measured abundances by their estimated average carbon content. This method was applied to the nine phytoplankton clusters characterized by Tzortzis et al. (2021). For the sake of simplicity, we regrouped the nine clusters by cell size into three phytoplankton groups:

1. Picophytoplankton, PICO ($< 2\mu m$)
2. Nanophytoplankton, NANO ($2 <$ and $< 20\mu m$)
3. Microphytoplankton, MICRO ($> 20\mu m$)

$$\text{BioV} = \text{FWS}^{\beta_1} \cdot e^{-\beta_0} \tag{1a}$$

$$Q_c = \alpha_0 \cdot \text{BioV}^{\alpha_1} \tag{1b}$$

$$\text{BioM} = \text{abundance} \cdot \bar{Q}_c \tag{1c}$$

The term "FWS" represents the ForWard Scatter, an optical measurement obtained by flow cytometry that is a proxy of the cell size. β_0 and β_1 are the parameters of the log-log regression between the FWS and the biovolume, with values of $\beta_0 = -5.8702$ and $\beta_1 = 0.9228$ (Tzortzis et al., 2023). α_0 and α_1 are parameters of the log-log regression between the biovolume and the carbon content (Table. 1).

2.2. Model description

The NP2Z model was developed for oligotrophic waters and is applied to the Mediterranean Sea. This simple model tests the bottom-up effect with

Table 1: Regression coefficients for the log-log relationship between biovolume and carbon content from the Table. 4 of Menden-Deuer and Lessard (2000).

	Menden-Deuer and Lessard (2000)	α_0	α_1
PICO	Protist plankton* (line 1)	0.210	0.939
NANO	Protist plankton (line 2)	0.260	0.860
MICRO	Diatoms (line 3)	0.287	0.811

a single nutrient to study species co-limitation, the top-down effect with one zooplankton, and observes transitions with two phytoplankton. The schematic diagram gives a pictorial view of trophic links between state variables and exchanges with the external environment (Fig. 1). The main assumptions used to construct the equations are as follows:

1. One limiting nutrient: in the Mediterranean Sea, phosphate is the key limiting nutrient (Moutin and Raimbault, 2002);
2. Fast organic matter dynamics and recycling: the detrital compartment and storage within the plankton are absent, and the uptake equation approximates Droop's growth model (Droop, 1983) using a Monod function (Monod, 1942). Dead phytoplankton cells do not sink, but are recycled directly into the phosphate compartment;
3. Two controls for the dynamics of phytoplankton: the growth limitation induced by the nutrient (bottom-up control) and the grazing limitation by zooplankton (top-down control).

The model equations are:

$$\frac{dPO_4}{dt} = P_{supply} + \epsilon_e(1 - \gamma)Z \sum g_i + \sum m_{P,i}P_i + \epsilon_n m_n Z - \sum \mu_i P_i \quad (2a)$$

$$\frac{dP_i}{dt} = \mu_i P_i - g_i Z - m_{P,i} P_i \quad (2b)$$

$$\frac{dZ}{dt} = Z\gamma \sum g_i - m_q Z^2 - m_n Z \quad (2c)$$

PO_4 stands for phosphate. $P_{i=1,2}$ stand for two phytoplankton groups, and Z stands for zooplankton. All state variables are masses expressed in $mmolC\,m^{-3}$, assuming a C:P molar ratio of 130:1 in phytoplankton in P-depleted conditions (Pulido-Villena et al., 2021).
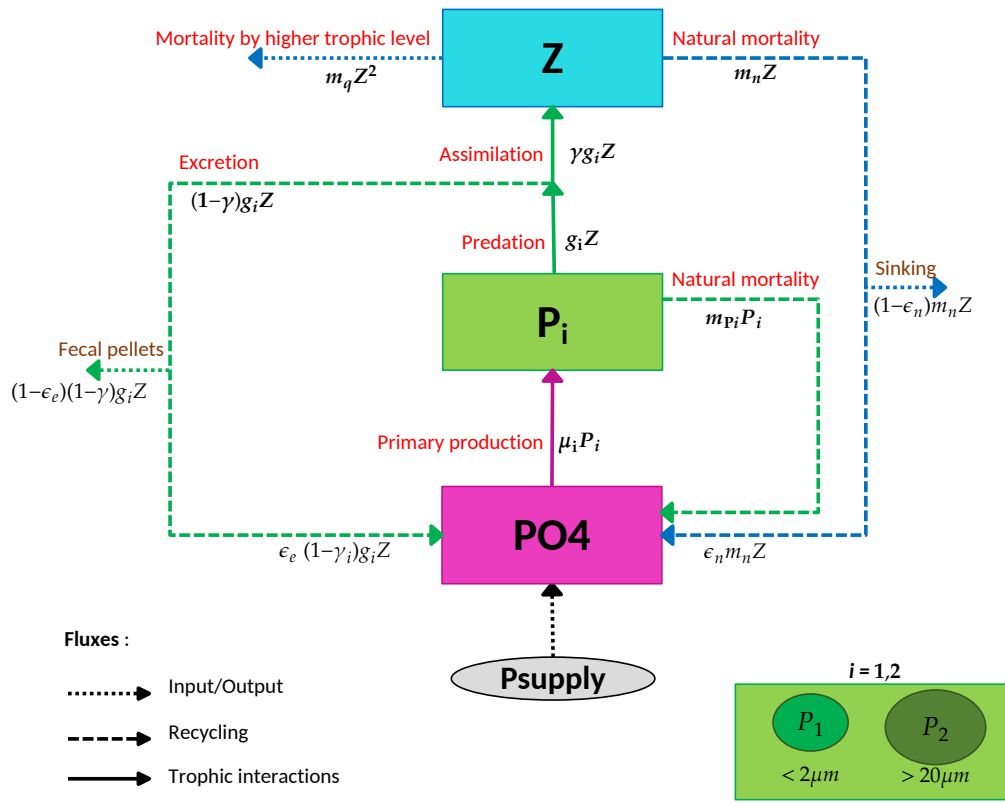
Figure 1: Model diagram. Model state variables are represented by boxes, biochemical processes by arrows and external forcing by an ellipse. All state variables are masses expressed in $mmol\,C\,m^{-3}$. Note that the colour code: magenta for PO_4, light green for P_1, dark green for P_2 and cyan for Z, is used throughout this paper.

The growth rate of phytoplankton class i (μ_i $[d^{-1}]$) is calculated from a Monod function:

$$\mu_i = \frac{PO_4}{PO_4 + K_{P,i}}\mu_{max,i} \tag{3}$$

The grazing rate of zooplankton on phytoplankton class i (g_i $[d^{-1}]$) is calculated according to the Holling type II response :

$$g_i = \frac{P_i}{P_1 + P_2 + K_{Z,i}}g_{max,i} \tag{4}$$

The detailed definitions of all parameters are provided in Table. 2. Parameter values were chosen based on the literature. The two phytoplankton size classes were parameterized to represent picophytoplankton (P1) and microphytoplankton (P2), which showed the highest contrast across the frontal region (Tzortzis et al., 2021). P_1, as a community of small species, is specialized in nutrient uptake in low-nutrient conditions ($K_{P,1} < K_{P,2}$) while P_2, as a community of larger species, is specialized in defense against predators ($g_{max,1} > g_{max,2}$). This implies that P_1 should dominate the community in nutrient-poor waters and P_2 should dominate the community in nutrient-rich waters (Thingstad and Rassoulzadegan, 1999; Bohannan and Lenski, 2000).

P_{supply} is the only external forcing in this study (Eq. 2a). A total phosphate supply in the south-western Mediterranean Sea of $0.0002\ mmol\,P\,m^{-3}\,d^{-1}$ was estimated during the 2017 PEACETIME cruise (Guieu and Desboeufs, 2017), corresponding to $0.03\ mmol\,C\,m^{-3}\,d^{-1}$ (Pulido-Villena et al., 2021). Given the limited availability of other *in situ* measurements in our study region, we assumed a P_{supply} range from a nutrient-poor to a nutrient-rich water mass between 0.01 and 0.10 $mmol\,C\,m^{-3}\,d^{-1}$, respectively.

2.3. Analysis

We conducted two analyses of the NP2Z model using numerical simulations based on Euler's explicit numerical scheme, with a 0.1-day time step. The first analysis focuses on constant forcing, examining equilibrium with all state variables as constants (obtained at 2000-day simulation cf. Fig. C.12 in Appendices). This helps elucidate factors influencing PCTs in each

8

Table 2: Model parameters with units, associated values and references

Symbol	Definition	Unit	Value	Reference
$\mu_{max,1}$	P_1 maximum growth rate	d^{-1}	1.9872	Baklouti et al. (2021)
$\mu_{max,2}$	P_2 maximum growth rate	d^{-1}	2.7648	Baklouti et al. (2021)
$g_{max,1}$	Z maximum grazing rate on P_1	d^{-1}	3.89	Auger et al. (2011)
$g_{max,2}$	Z maximum grazing rate on P_2	d^{-1}	0.43	Auger et al. (2011)
$K_{P,1}$	P_1 half-saturation constant	$mmolC\,m^{-3}$	1	This article
$K_{P,1,litt}$	Half-saturation constant of *Synecho.* and small phyto resp.	$mmolC\,m^{-3}$	1.82, 6.5	Timmermans et al. (2005), Munkes et al. (2021)
$K_{P,2}$	P_2 half-saturation constant	$mmolC\,m^{-3}$	3	This article
$K_{P,2,litt}$	Half-saturation constant of *A. formosa* and diatoms resp.	$mmolC\,m^{-3}$	2.6, 13	Grant (2014), Munkes et al. (2021)
$K_{Z,1}$	Z half-saturation constant for P_1	$mmol\,Cm^{-3}$	5	Auger et al. (2011)
$K_{Z,2}$	Z half-saturation constant for P_2	$mmolC\,m^{-3}$	20	Auger et al. (2011)
$m_{P,1}$	P_1 mortality rate	d^{-1}	0.10	This article
$m_{P,1,litt}$	Mortality rate of P_1 in litterature	d^{-1}	0.07, 0.16	Baklouti et al. (2021), Auger et al. (2011)
$m_{P,2}$	P_2 mortality rate	d^{-1}	0.2	This article
$m_{P,2,litt}$	Mortality rate of P_2 in litterature	d^{-1}	0.1, 0.10	Baklouti et al. (2021), Auger et al. (2011)
m_n	Z natural mortality rate	d^{-1}	0.10	Auger et al. (2011)
m_q	Z quadratic mortality rate	$m^3(mmol\,Cd)^{-1}$	0.061	Auger et al. (2011)
γ	Conversion coefficient from P to Z	-	0.6	Auger et al. (2011)
ϵ_n	$PO4$ Z natural mortality recycling coefficient	-	0.3	This article
ϵ_e	$PO4$ Z excretion recycling coefficient	-	0.7	Baklouti et al. (2021)
P_{supply}	Phosphate supply	$mmolC\,m^{-3}\,d^{-1}$	/	/

water mass on either side of the frontal area, assuming a homogeneous environment with a constant phosphate supply. The second analysis focuses on pulsed forcing, examining the state variables response after a perturbation. This helps to elucidate factors influencing PCTs in a variable environment, considering a front and assuming pulsed phosphate supplies.

2.3.1. Constant forcing

We analyzed the model using a simpler version to understand its qualitative behavior, specifically focusing on the role of P_{supply}. This simplified formulation was achieved by assuming that concentrations are small relative to half-saturation constants, which lets us approximate equations by removing the variable denominator in the growth rate and grazing rate functions (Eq. 5 and Eq. 6).

Eq. 3 becomes:

$$\mu_i = \frac{PO_4}{K_{P,i}}\mu_{max,i} \tag{5}$$

Eq. 4 becomes:

$$g_i = \frac{P_i}{K_{Z,i}}g_{max,i} \tag{6}$$

The full model was numerically analyzed to study the evolution of the state variable depending on different constant values of P_{supply}. The equilibrium state was reached, for a 2000-days simulation, by applying a constant
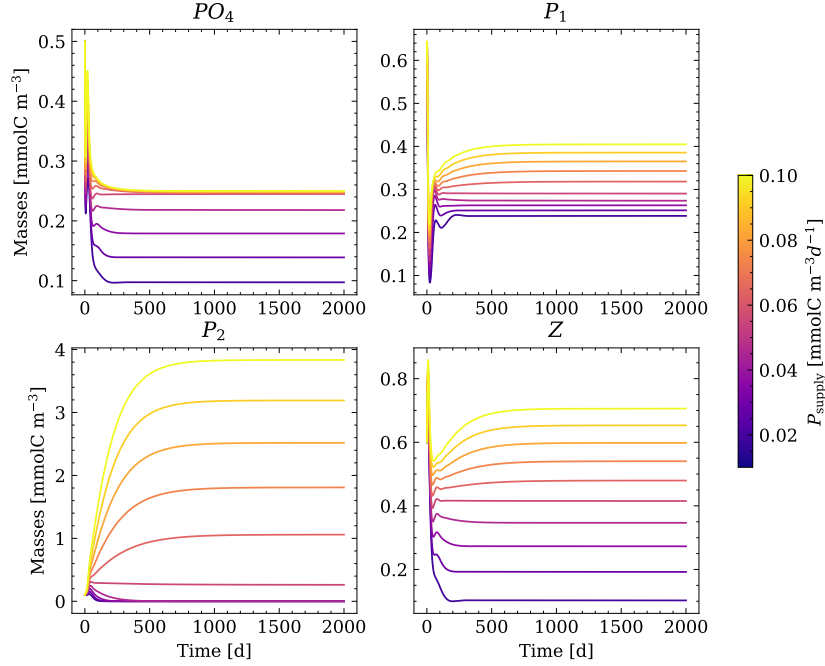
Figure 2: Temporal evolution of individual state variables, with lines colour-coded based on their forcing parameter (P_{supply}), ranging from 0.01 to 0.10 $mmolC\,m^{-3}d^{-1}$ in 10 increments.

value of P_{supply} within the above-mentioned range initiated from the following set of values : $PO_4 = 0.5$, $P_1 = 0.6$, $P_2 = 0.1$, $Z = 0.6\,[mmolC\,m^{-3}]$.

We plotted the model's temporal evolution to confirm its constancy within the P_{supply} range. Fig. 2 shows equilibrium for 10 values of P_{supply}.

The Jacobian matrices associated with each equilibria found for the simplified model and the full model were calculated. The dominant eigenvalue of the matrices (complex number, termed λ_{max}) indicates the stability with which perturbations propagate around an equilibrium. If the real part of the dominant eigenvalues is negative, the equilibrium is stable, if not the equilibrium is unstable. The calculation of eigenvalues for different values of P_{supply} within the range defined above, were then used to construct bifurcation diagrams, enabling us to explore how equilibria interact and evolve with different values of P_{supply}. We focus solely on positive equilibria, ensuring realistic values for state variables.

10

Several tests on the full model were carried out to justify the choice of differential grazing on P_1 and P_2: A "No grazing" test, i.e. $Z = 0$ and an "Equal grazing" test, i.e. $g_{max,1} = g_{max,2} = 3.89\,[d^{-1}]$, $K_{Z,1} = K_{Z,2} = 5\,[mmolC\,m^{-3}]$. Then, the "Differential grazing" test was implemented with the parameters shown in Table. 2, for the simple and full models.

Full model sensitivity to parameters under constant forcing was tested following the method used by Messié and Chavez (2017). We examined the effect of varying values of $u_{max,i}, K_{P,i}, g_{max,i}$ and $K_{Z,i}$, as these parameters dictate bottom-up and top-down forcing on each phytoplankton, ultimately controling their relative proportions. For each parameter, three runs were performed using i) the default parameter value (Table. 2), ii) half of the default value and iii) twice the default value, while maintaining the others parameters at their default value. The percentage of variation represents the difference between the outcomes of the third and second runs, divided by the result of the first (average value of the last 200 values in a 2000-day simulation). A positive variation percentage signifies the second run's value is higher than the third run's value, while a negative percentage indicates the opposite. This analysis was conducted for the two values of P_{supply} defining the nutrient-poor ($P_{\text{supply}} = 0.01\ mmolC\,m^{-3}\,d^{-1}$) and nutrient-rich ($P_{\text{supply}} = 0.10\ mmolC\,m^{-3}\,d^{-1}$) water masses for a total of 8 (parameters) x3 (runs) x2 (P_{supply}) simulations. Figures D.13 and D.14 in the Appendices show the temporal evolution of state variables at each runs.

2.3.2. Pulsed forcing

To simulate fluctuating forcing within a front, a pulsed P_{supply} was implemented as:

$$P_{\text{supply}}(t) = b \cdot (U(t - t_1) - U(t - t_2)) + P_{\text{supply},0} \qquad (7)$$

where:

- b is the amplitude of the pulse

- t_1 is the start time of the pulse

- t_2 is the end time of the pulse

- $P_{\text{supply},0}$ is the value of P_{supply} at $t = 0$

11

- $U(x)$ is the step function (or Heaviside function) defined as:

$$U(x) = \begin{cases} 0 & \text{if } x < 0 \\ 1 & \text{if } x \geq 0 \end{cases}$$

This analysis aims to assess the repercussions of a phosphate pulse on PCTs in comparison to the constant forcing analysis. We investigate the effect of amplitude and number of pulses on the temporal evolution of the state variables. The analysis started with the coexistence of both phytoplankton species in equivalent proportion, obtained with $Psupply, 0$.

The software developed for this work, containing the NP2Z model as well as all the calculations described above, is available on a GitHub repository: https://github.com/OmsLaurina/toolbox_growthmodel.

3. Results

3.1. In situ observations

Fig. 3 displays the biomass of the three phytoplankton size groups at each sampling point. Contrasted biomasses are observed across latitude 38.5°N, which was identified as the position of a front between two water masses of different origins (Tzortzis et al., 2021).

For each three phytoplankton size group we calculated the ratio between the average biomass in the south ($BioM_{S,j}$ [$mmolC\,m^{-3}$]) and the north ($BioM_{N,j}$ [$mmolC\,m^{-3}$]) with respect the front position to determine the observed increase/decrease biomass factor ($f_{BioM,j}$ [/]) (Eq. 8). If $f_{BioM,j} > 1$ this means that the biomass in the south is greater than the biomass in the north, and vice versa if $f_{BioM,j} < 1$.

$$f_{BioM,j} = \frac{\overline{BioM_{S,j}}}{\overline{BioM_{N,j}}} \tag{8}$$

Where $j = PICO, NANO, MICRO$.

The PICO group was more represented in southern waters ($f_{BioM,PICO} > 1$), while the MICRO group was more represented in northern waters ($f_{BioM,MICRO} < 1$). However, the NANO group was almost as well represented in the south as in
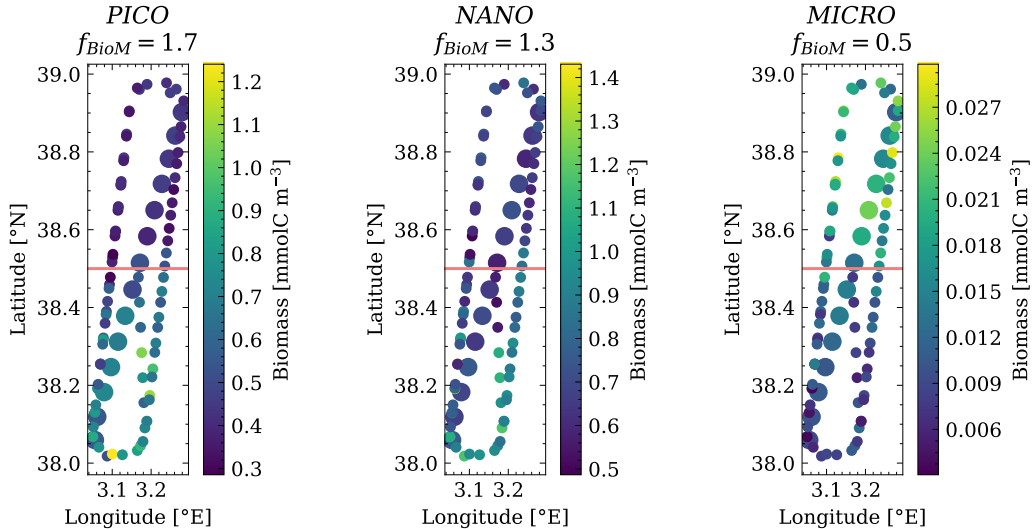
Figure 3: *In situ* measurements of PICO (left panel), NANO (middle panel), and MI-CRO (right panel) biomasses across the hippodrome during the PROTEVSMED-SWOT campaign. The coral line represents the estimated position of the front. The value of the biomass factor $f_{BioM,j}$ of each group is reported at the top of each subplot. The larger dots represent the transect shown by Tzortzis et al. (2021) and corresponding to the sampling period 11-May-2023 02:00 to 11-May-2023 08:40.

the north ($f_{BioM,NANO}$ close to 1). The NANO biomass comprises two groups: NANO1, more abundant in the southern frontal zone ($f_{BioM,NANO1} = 1.62$), and the larger NANO2, which does not show a particular distribution ($f_{BioM,NANO2} = 1.01$).

3.2. Numerical simulations with constant forcing

Analytical calculations and numerical simulations were carried out to study the stability of the model equilibria. Fig. 4 shows the bifurcation diagrams for both the simplified and full models.

With the simplified model (panel a.) we analytically found two equilibria, each one corresponding to the absence of one of the two phytoplankton groups. The first equilibrium $\bar{X}_1$ ($P_2 = 0$) is stable up to a value of P_{supply} of 0.055 (i.e. the bifurcation point), while the second equilibrium $\bar{X}_2$ ($P_1 = 0$) is the opposite. Using the full model (panel b.), we analytically identified two equilibria, each associated with the absence of one of the two phytoplankton groups. The first equilibrium $\bar{Y}_1$ ($P_2 = 0$) is stable up to a value
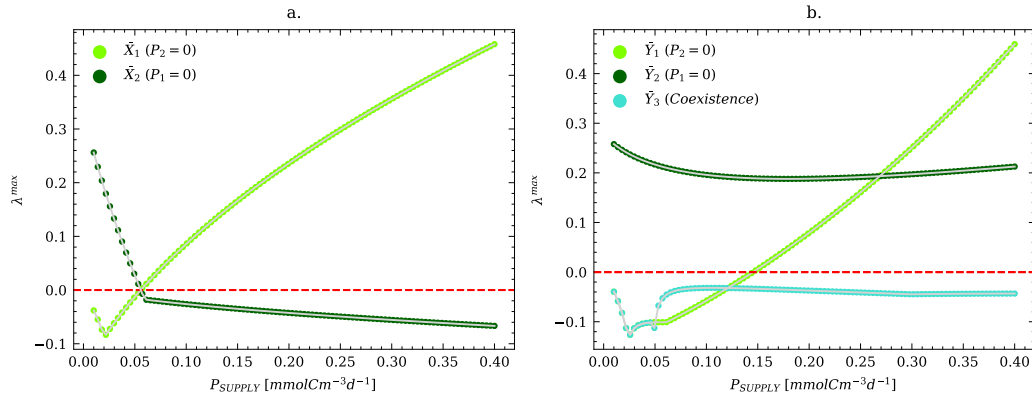
13

Figure 4: Bifurcation diagrams representing the dominant eigenvalue λ_{max} calculated for phosphate supply P_{supply} ranging between 0.01 and 0.40 $mmolC\,m^{-3}d^{-1}$. Panel a. shows the results of the simplified model: the light green line represents the first equilibrium ($\bar{X}_1$) and the dark green line represents the second equilibrium ($\bar{X}_2$). Panel b. shows the results of the full model: the light green line represents the first equilibrium ($\bar{Y}_1$), the dark green line represents the second equilibrium ($\bar{Y}_2$) and the turquoise line represents the third equilibrium ($\bar{Y}_3$). The dotted red lines represent $\lambda_{max} = 0$. Equilibria are stable when curves are below this red line ($\lambda_{max} < 0$), and unstable when curves are above this red line ($\lambda_{max} > 0$). Bifurcation points correspond to the intersection between the curves and the red line.

of P_{supply} of 0.140 $mmolC\,m^{-3}d^{-1}$ (i.e bifurcation point), while the second equilibrium $\bar{Y}_2$ ($P_1 = 0$) is never stable. Additionally, we numerically determined one equilibrium representing the coexistence of both phytoplankton groups. The coexistence equilibrium is always stable, but negative for $P_{\text{supply}} < 0.045\,mmolC\,m^{-3}d^{-1}$ (irrelevant to our investigation). The positive equilibrium is achieved when P_{supply} exceeds 0.045 $mmolC\,m^{-3}d^{-1}$, with the initial set of state variable values (section 2.3.1).

3.2.1. Bottom-up vs top-down controls

We explored the role of bottom-up and top-down controls by calculating the equilibrium values of the system after 2000 days of simulations within the P_{supply} range from 0.01 to 0.10 $mmolC\,m^{-3}d^{-1}$, and defining the R-ratio as:

$$0 \leq R = \frac{P_1}{P_1 + P_2} \leq 1 \tag{9}$$

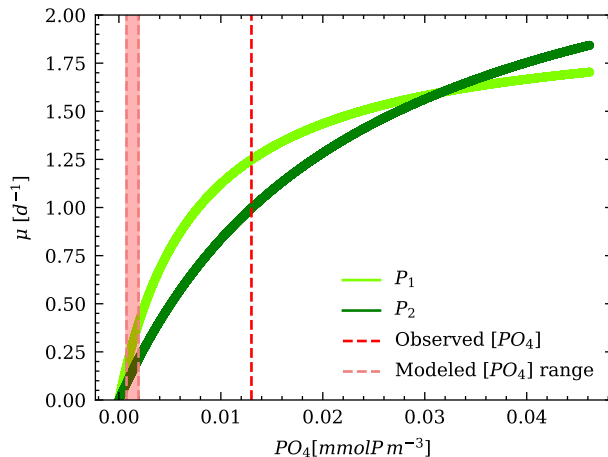By definition R-ratio is equal to 0 if $P_1 = 0$ and equal to 1 if $P_2 = 0$.

14

Figure 5: Theoretical Monod curves representing the growth rates of P_1 and P_2 as a function of PO_4 concentration. The shaded area in light red depicts the portion of Monod curves that is constrained by model-predicted values of P_{supply} ranging from 0.01 to 0.10 $mmol\,C\,m^{-3}d^{-1}$. The concentrations of PO_4 range from 7.10^{-4} to 0.002 $mmol\,P\,m^{-3}$. The dashed line in dark red corresponds to the average concentration of 0.013 $mmol\,P\,m^{-3}$ measured by (Pulido-Villena et al., 2021) in the south-western Mediterranean Sea.

Fig. 5 shows the Monod curves representing the nutrient uptake kinetics of P_1 and P_2. The growth rate of P_2 is higher than for P_1 when the PO_4 concentration is above 0.03 $mmol\,P\,m^{-3}$. This implies that PCTs would happen at PO_4 concentrations much higher not only than the modeled ones (shaded area) but also than ones observed by Pulido-Villena et al. (2021) (dashed red line).

We assessed the influence of top-down forcing performing simulations without grazing ("no grazing test") and without differential predation ("equal grazing test") (Fig.A.10). The "no grazing test" demonstrates the importance of the presence of zooplankton for observing PCTs: without zooplankton grazing, P_1 increases indefinitely, no equilibrium is reached and R-ratio is always equal to 1. With the same grazing pressure on both phytoplankton groups, we obtained an equilibrium, but no coexistence. Indeed, P_2 disappears very rapidly and R-ratio becomes equal to 1. These tests demonstrate that differential grazing is necessary to reach equilibria with P_2 survival (R-ratio < 1).
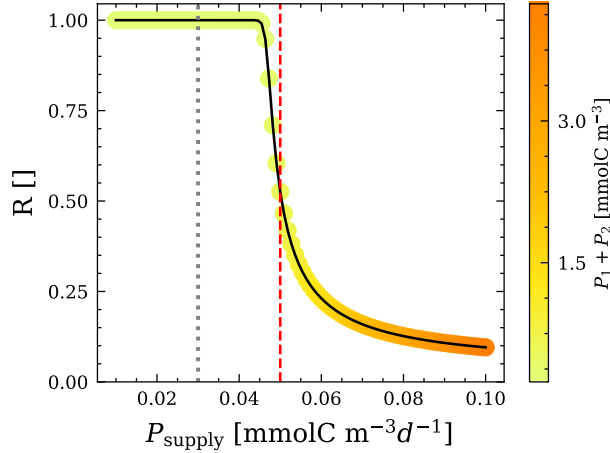
15

Figure 6: R-ratio as a function of different values of P_{supply}. The colour bar represent the total biomass $(P_1 + P_2)$. The dashed red line corresponds to the value of P_{supply} where the R-ratio closest to 0.5 (i.e. when P_1 and P_2 are in close proportions), and the dotted gray line correspond to the P_{supply} measured by Pulido-Villena et al. (2021).

Fig. 6 shows the influence of P_{supply} on system equilibria using the R-ratio and now considering the differential grazing pressure. With low (high) values of P_{supply}, P_1 (P_2) largely dominates and R-ratio tends to 1 (0). The transition point, i.e. the value of P_{supply} where R-ratio becomes inferior to 0.5, is reached for P_{supply} equal to $0.050\ mmolC\,m^{-3}d^{-1}$. Note that both PO_4 and Z increase with P_{supply}.

3.2.2. Sensitivity analysis

Fig. 7 summarizes the results of the sensitivity analysis of the state variables PO_4, P_1 and P_2, together with the derived variable R-ratio, to the main model parameters. P_{supply} being the main driving parameter, we separate the figure in two plots corresponding to the extreme values of P_{supply} used in this work. Note that at steady state Z is independent of parameters and only function of P_{supply} due to the equilibrium between P_{supply} and the three sink terms, fecal pellets, sinking and quadratic mortality, hence Z is not shown in Fig. 7.

For low values of P_{supply} (left panel), the percentage variation of PO_4 is positive for $K_{P,1}$ and $g_{max,1}$ and negative for $\mu_{max,1}$, which is the most sensible parameter, and $K_{Z,1}$. Instead, the percentage variation of P_1 is negative for
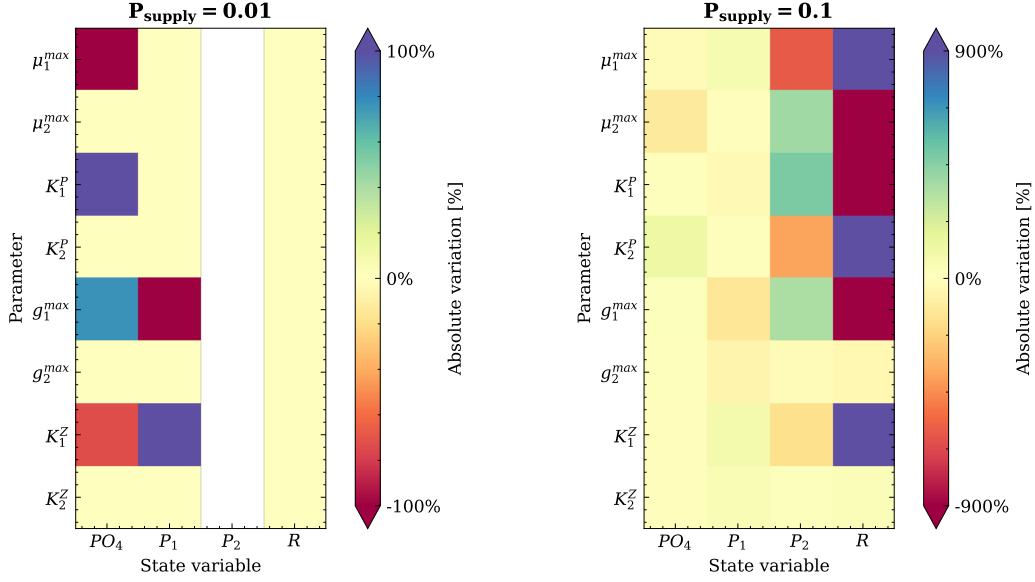
16

Figure 7: Sensitivity analysis of key parameters on state variables. The left panel corresponds to the simulations with P_{supply} equal to 0.01 $mmolC\,m^{-3}d^{-1}$, and the right panel corresponds to the simulations with P_{supply} equal to 0.10 $mmolC\,m^{-3}d^{-1}$. The colours represent the absolute percentage variation from the default value of the state variables. The white colour for P_2 represents NaN values due to division by 0 (P_2 is equal to 0 for all runs at P_{supply} equal to 0.01 $mmolC\,m^{-3}d^{-1}$).

$g_{max,1}$ and positive for $K_{Z,1}$. For high values of P_{supply} (left panel), PO_4 and P_1 generally show a much lower sensitivity with respect to P_2 and, as a consequence, R-ratio. The percentage variation of P_2 is mainly negative for $\mu_{max,1}$ and $K_{P,2}$. R-ratio is sensitive to all parameters except $g_{max,2}$ and $K_{Z,2}$; the others parameters generate variations of over 1000%, i.e. 20 times more than the default value. Details of each parameter's effect for each run are outlined in Fig. D.13 and Fig. D.14. Oscillations around the equilibrium value were observed for PO_4 when $P_{\text{supply}} = 0.1\,[mmolC\,m^{-3}d^{-1}]$ (Fig. D.14).

3.3. Pulsed forcing

To simulate the frontal region, where the 3D fine-scale dynamics can generate vertical nutrient injections, we introduced one to three P_{supply} pulses with varying intensities and we analyzed state variables and the R-ratio over a 90-day simulation. Initial conditions were set to the model steady-state outputs corresponding to P_1 and P_2 coexisting in equivalent proportion (ob-

17

tained with $P_{supply,0} = 0.050 \, [mmolC \, m^{-3} d^{-1}])$.

Except for the case of a single weak pulse with very low fluxes, moderate impulsive fluxes or/and multiple pulses generate transitions with P_2 becoming dominant with time. For all three simulations (from one to three pulses), the concentration of PO_4 increases after each pulse and then sharply decreases as it is consumed by phytoplankton (Fig. 8, top panels). At the end of the simulations, both phytoplankton groups still coexist, but P_2 is dominant. The dominance by P_1, as summarized by the R-ratio, depends on the pulse amplitude (Fig. 8, middle panels). However, the timing of transitions remains similar across a range of pulse amplitudes: P_1 dominates until about 20 days, with a peak concentration just after P_{supply} pulses, then the system switches from P_1 to P_2 from 20 to 40 days. The presence of additional pulses shortens the transition phase, leading P_2 to dominate more, while P1 tends to return to its initial concentration. (Fig. 8, middle panels). Zooplankton biomass is always maximum during the periods of transition from P_1 to P_2 (Fig. 8, bottom panels). The minimum R-ratio value and the maximum Z biomass achieved after pulses are both enhanced with increasing pulse amplitude.

4. Discussion

The cytometry measurements conducted during the PROTEVSMED-SWOT cruise showed contrasted phytoplankton abundances and biomasses in two distinct water masses separated by a front, with the smaller (larger) phytoplankton dominating south (north) of the front (Tzortzis et al., 2021, and Fig. 3). Using a size-structured population model, Tzortzis et al. (2023) showed that observed contrasted abundances across the front were associated with different growth and loss rates. However, open questions remained, mainly due to the lack of both nutrient and grazing measurements. Here, we developed an NP2Z model to understand the community dynamics and better explain the observations. We categorized the phytoplankton groups identified by cytometry in two size groups: small phytoplankton P_1 and large phytoplankton P_2. We hypothesized that fine-scale dynamics, involving hydrodynamic barriers and variations in phosphate flux pulses, generate spatial and temporal PCTs on P_1 and P_2. We considered two scenarios: a homogeneous environment representing water masses on each side of the front and a variable environment representing the frontal area. In the following, we suc-
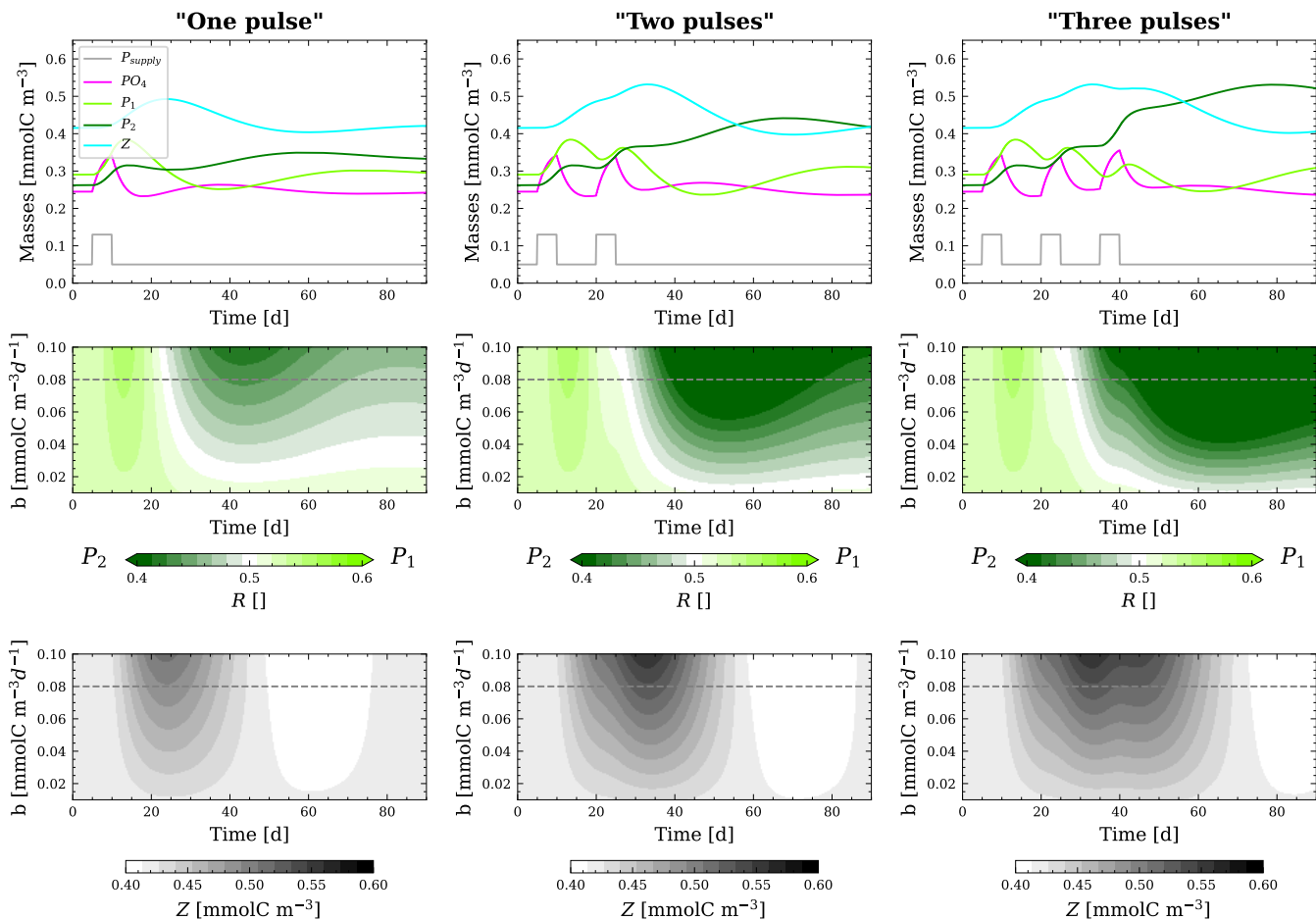
Figure 8: Response of state variables and R-ratio to a different number of pulses and different amplitudes of P_{supply} over 90-day simulations. The results of the simulations with one, two and three pulses are shown in the left, middle and right columns, respectively. The upper row shows the time evolution of state variables for a pulse amplitude $b = 0.08\,[mmolC\,m^{-3}d^{-1}]$. The middle row shows the R-ratio as a function of the time and the pulse amplitude. The bottom row is the same as the middle one but for Z. The dotted grey lines correspond to the simulation with a pulse amplitude $b = 0.08\,[mmolC\,m^{-3}d^{-1}]$.

19

cessively consider hypotheses of bottom-up and top-down controls on PCTs in each scenario.

4.1. Driving mechanisms beyond P_{supply} in homogeneous environments

Our simulations show that P_{supply} drives PCTs (Fig. 4 and 6). A bottom-up control via changes in nutrient fluxes thus seems like a logical hypothesis to explain PCTs. However, Monod curves indicate that increased P_{supply} within a realistic range for the oligotrophic ocean promotes P_1 growth but does not allow PCTs (Fig. 5, shaded red area). Note that the modeled PO_4 concentrations are lower than observed, possibly due to the absence of a detrital compartment in the model (Edwards, 2001). Grover (1990) demonstrated in a Nutrient-Phytoplankton model that, in a homogeneous environment, species with the highest maximum growth rate dominate in competition when resources are sufficiently abundant. However, our field observations suggest a more frequent occurrence of coexistence rather than competitive exclusion. Taken together, these results indicate that the observed PCTs on either side of the front cannot be solely attributed to bottom-up control.

Therefore, we explored the top-down process of zooplankton grazing. Adding grazing, our model reaches equilibrium, leading to stable concentrations and the coexistence of P_1 and P_2. Indeed, grazing is known to play a pivotal role in stabilizing the model and allowing coexistence, while nutrient limitation restrain it (Ward et al., 2014). When grazing rates are equal, the model attains only one equilibrium, resulting in the complete dominance of P_1 while P_2 goes fast to 0 (Fig. B.11 in Appendices).

To reproduce the observed PCTs, differential grazing rates need to be introduced. Different grazing forcing configurations are considered as a key factor in creating phytoplankton successions and structuring communities during blooms (Prowe et al., 2012). We introduced the differential grazing in the simplified model that shows a transcritical bifurcation for P_{supply} equal to $0.055 \ mmolC \, m^{-3} d^{-1}$ (Fig. 4a.). This latter value, identified analytically, is called the "dominance threshold". A similar value of $0.050 \ mmolC \, m^{-3} d^{-1}$ of dominance threshold, was found numerically for the full model (Fig. 4b. and 6). With the full model we also identified a threshold value of 0.045 $mmolC \, m^{-3} d^{-1}$ above which both phytoplankton coexist in the system, called the "coexistence threshold". These results show that differential grazing is key to obtaining PCTs, and that P_{supply} is the main control parameter. This

20

means that, in a homogeneous environment, PCTs are determined by the interplay of bottom-up and top-down controls.

4.2. Driving mechanisms beyond P_{supply} in a variable environment

To assess the effectiveness of combined bottom-up and top-down controls in a variable environment, we simulated pulsed nutrient fluxes. Our results show that one or multiple pulses generate temporal successions between P_1 and P_2 leading to both short-term and delayed temporal PCTs (Fig. 8). This is consistent with freshwater systems where Yamamoto and Hatta (2004) showed that nutrient pulses also cause different species-dependant responses in the phytoplankton community. The temporal transitions between P_1 and P_2 are linked to the pulse characteristics, such as the amplitude and the number of pulses. We can then transpose our results to the case of fine-scale frontal areas, where the predominance of fast-growing groups like P_2 is explained by nutrient enrichment (Mangolte et al., 2023). However, because the dominance threshold coincides with the zooplankton peak, we attribute the end-of-simulation dominance of P_2 to the "shared predator" concept by Mangolte et al. (2022) where increased phytoplankton biomass, following nutrient input, raises the common phytoplankton predator's biomass. During the dominance threshold time, P_1 is more grazed than P_2, favoring the latter and creating PCTs. Our results also showed a lack of competitive exclusion: both phytoplankton groups coexist for all three sets of simulations. Previous *in situ* observations showed that the front increases the biomass of several phytoplankton groups and not just diatoms (Mangolte et al., 2023). Our study reveals that even in a variable environment PCTs are influenced by the synergy of bottom-up and top-down controls which also act as a function of the number of pulses and their intensity.

4.3. A theoretical framework to fine-scale observations

Fig. 9 summarizes both in situ observations (top panel) and modelling results (bottom panel). The *in situ* R-ratio was computed from PROTEVSMED-SWOT cruise data by dividing the biomass of PICO and NANO1 cytometric groups by the total biomass at each sampled point. The scatter plot clearly depict the shift from smaller phytoplankton dominance in the south to larger phytoplankton dominance in the north. The steepest gradient is located at latitude 38.5°N, identified as the position of the front separating two different water masses (Tzortzis et al., 2021). In the south, there was Atlantic water that recently entered the Mediterranean, while the north

exhibited saltier surface water from the western Mediterranean circulation. This circulation is known to enrich the surface water in nutrients (Millot and Taupier-Letage, 2005). Despite the absence of nutrient measurements during the PROTEVSMED-SWOT cruise, our model, linking nutrient supply to the transition to larger phytoplankton, generally explains the observations well, except for the *in situ* total biomass which is lower in the north, contrary to observations. We attributed this discrepancy to limitations of the cytometry methodology, causing an underestimation of the abundance and size of the MICRO group, which makes a significant contribution to biomass. Indeed, flow cytometers are known to provide less accurate counts of large cells (Cunningham and Buonnacorsi, 1992; Peperzak et al., 2018). Satellite-derived chlorophyll surface concentration was higher in the north (Fig. 9, top panel), in agreement with the model results.

Despite its simplifications the model allows us to better understand the mechanism underlying the observations, illustrated in Fig. 9 (bottom panel). In nutrient-poor waters (left side), P_1 dominates due to its higher growth rate at low nutrients concentrations. By increasing P_{supply}, it reaches a level allowing the emergence of P_2, i.e. the coexistence threshold. Zooplankton then influences both phytoplankton groups, with a higher grazing pressure on P_1. Both phytoplankton thrive more at a higher value of P_{supply}, but P_1 is grazed more, leading to the dominance of P_2 beyond the dominance threshold. This threshold is positioned close to the part of the curve where the slope is maximal, aligned with the observation that fronts are regions of strong gradients. Our results confirm the structuring effect of fine-scale fronts on the plankton community created by both pulsed nutrient supply and separated fluid dynamical niches (Lévy et al., 2018; d'Ovidio et al., 2010). These fine-scale contrasts resemble large-scale contrasts. Indeed, the research by Dutkiewicz et al. (2024) demonstrates that biotic interactions are influenced by gradients in resource supply and the ratio of multiple resource supplies across large-scale transition zones.

4.4. Model caveats

Our study of PCTs relies on a strongly simplified model. Another approach could have used more complex modelling with multiple plankton groups and nutrient pools. These models incorporate the effects of temperature as well as the dynamics of the microbial loop, among others (e.g. in the Mediterranean Sea, Auger et al., 2011; Aumont et al., 2015; Baklouti
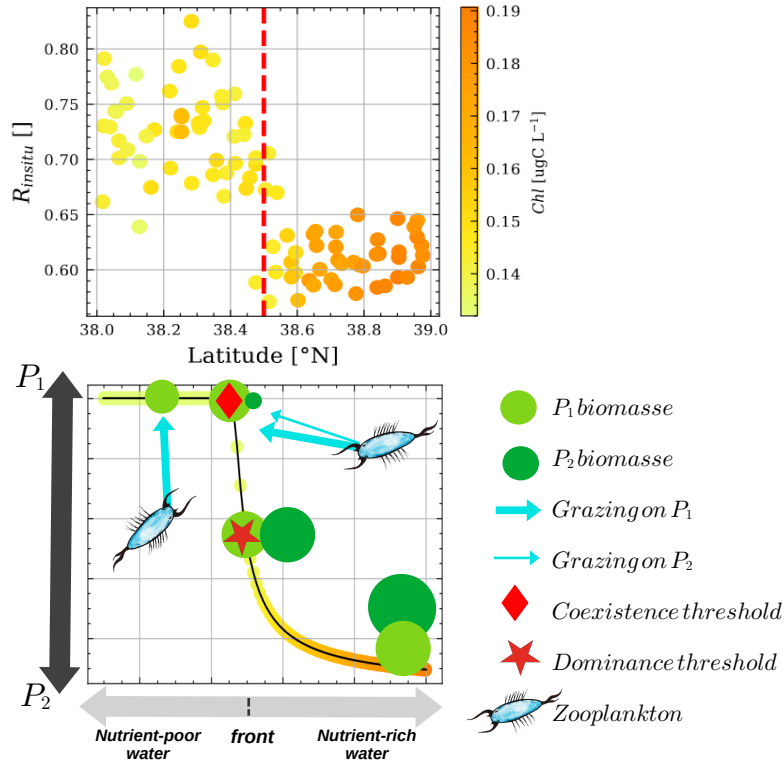
Figure 9: Top panel: the *in situ* R-ratio, calculated by dividing the biomass of the PICO and NANO1 cytometry groups by the total biomass at each measured points, is plotted as a function of the latitude. The black line the polynomial regression (third-order). The colours represent the total biomass of each point. The dotted red line represents the position of the frontal area (Tzortzis et al., 2021). Scatter size corresponds to normalized chlorophyll concentration. Bottom panel: the schematic illustrates the proposed mechanism explaining the observed phytoplankton distribution in the two adjacent water masses.

et al., 2021). Nevertheless, simple models are able to represent the global ecosystem features described by a complex model (Raick et al., 2006) with the advantage of being easier to interpret. Indeed, foundational principles are identical and qualitative behaviors are similar in both simple and complex models (e.g., Behrenfeld and Boss (2014)). Moreover, our results are consistent with results obtained from more complex models, including the fact that the composition of the community structure is explained by the synergy of bottom-up and top-down controls (e.g. Sailley et al., 2013). More recently, Mangolte et al. (2023), using an ecosystem model including multiple functional groups and sizes of plankton and coupling it with a circulation model, showed that the planktonic ecosystem response to enhanced nutrient supply at fronts is more complex than the pure bottom-up response because of ecological interactions such as shared predation, as we found with our simplified model.

5. Concluding remarks and perspectives

Within a theoretical framework, we explored the phytoplankton community transitions (PCTs) observed during the PROTEVSMED-SWOT cruise. The question, "How do fine-scale dynamics explain PCTs?", is answered by fine-scale dynamics shaping the nutrient seascape and creating PCTs via cascading effects of nutrient transfer through the plankton food chain. The phytoplankton uptake at different nutrient supply levels combined with the grazing forcing generates the coexistence and dominance thresholds. PCTs occur at the scale of water masses, where constant P_{supply} conditions lead to spatial PCTs, and also at the scale of fronts, where variable P_{supply} conditions lead to temporal PCTs. Comparison with *in situ* data validates the use of such a simple model to study PCTs in terms of qualitative behaviors. These results, derived from simple formulations, help us understand the much more complex behavior of phytoplankton cells adapted to fine-scale habitats. In future studies, this model will be spatialized and enhanced with high-resolution data from the BioSWOT-Med cruise (Doglioli and Gregori, 2023). The goal will be to study the fine-scale dynamics of plankton communities using a Lagrangian framework, adapting the growth-advection method (Messié et al., 2022) for oligotrophic areas like the Mediterranean Sea.

6. Acknowledgments

7. Funding

Appendix A. "No grazing"

When Z is set to 0 in the complete model, no equilibria were identified. Fig. A.10 illustrates that in the absence of grazing, the P_1 biomass increases infinitely over time for P_{supply} values of 0.01 and 0.10 $mmolC\,m^{-3}d^{-1}$. The same figure highlights that coexistence is unattainable without grazing, evidenced by a constant R-ratio of 1 across the entire P_{supply} range.

Appendix B. "Equal grazing"

When Z is set equal for P_1 and P_2 in the complete model, equilibria were identified. Fig. B.11 illustrates that in the presence of equal grazing, all masses reaches equilibrium over time for P_{supply} values of 0.01 and 0.10 $mmolC\,m^{-3}d^{-1}$. However, the same figure highlights that coexistence is unattainable with equal grazing, as evidenced by a constant R-ratio of 1 across the entire P_{supply} range.
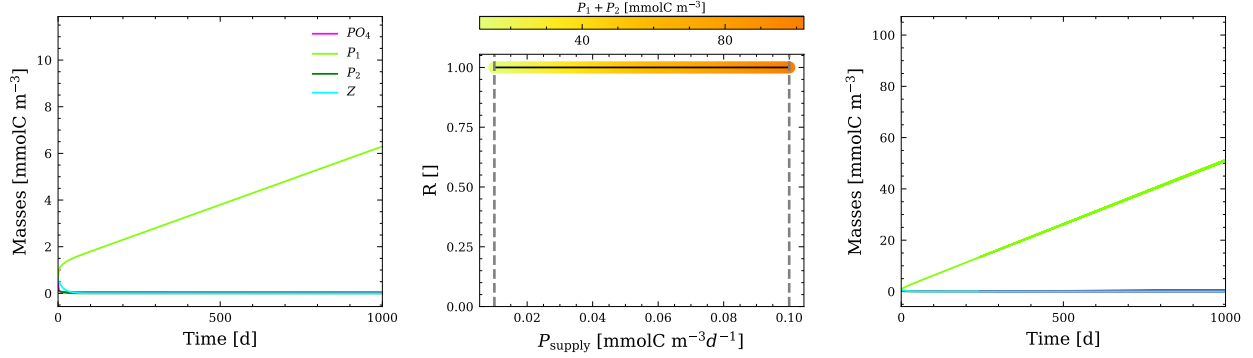
Figure A.10: Temporal evolution of state variables and R-ratio as a function of different values of P_{supply} for the "No grazing" test. The middle panel shows the evolution of the R ratio as a function of the range of P_{supply} values. The left and right panels show the temporal variation of state variables for a specific P_{supply} value of 0.01 $mmolC\,m^{-3}d^{-1}$ (left) and 0.10 $mmolC\,m^{-3}d^{-1}$ (right), indicated by the grey dotted line in the middle graphs.
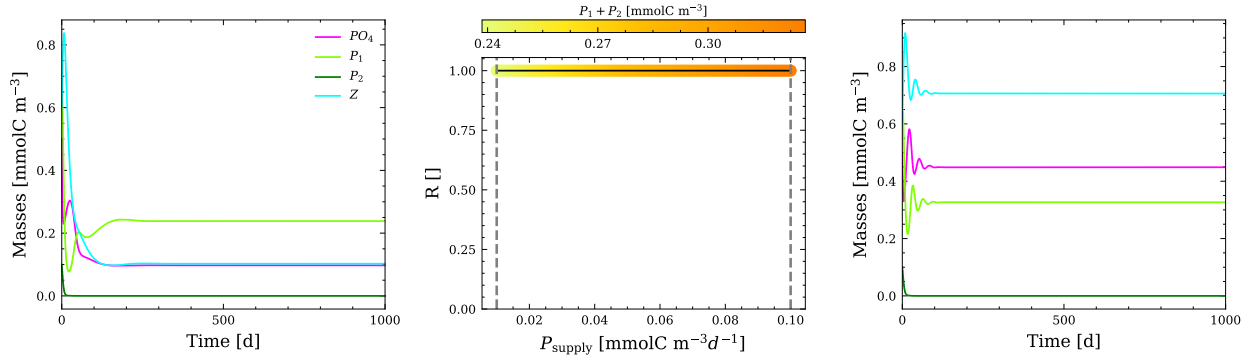

Figure B.11: Temporal evolution of state variables and R-ratio as a function of different values of P_{supply} for the "Equal grazing" test. The middle panel shows the evolution of the R ratio as a function of the range of P_{supply} values. The left and right panels show the temporal variation of state variables for a specific P_{supply} value of 0.01 $mmolC\,m^{-3}d^{-1}$ (left) and 0.10 $mmolC\,m^{-3}d^{-1}$ (right), indicated by the grey dotted line in the middle graphs.

Appendix C. "Differential grazing"

When Z is differentially set for P_1 and P_2 in the complete model (with a preference for P_1), equilibria were identified. Fig. C.12 illustrates in the phase space that in the presence of differential grazing, the system reaches equilibrium across the entire P_{supply} range, allowing for coexistence between P_1 and P_2. The values of these equilibria vary based on the P_{supply} value.

Appendix D. Sensitivy test

The sensitivity analysis indicates that specific parameters exert notable effects on state variables, with a more pronounced effect observed when P_{supply} is set to 0.10 $mmolC, m^{-3}d^{-1}$. These results are associated with the interplay between nutrient availability, P_1 uptake, and P_2 uptake.

Fig. D.13 illustrates the temporal evolution of eight parameters across three runs, with P_{supply} set to 0.01 $mmolC, m^{-3}d^{-1}$. Notably, changes in parameter values primarily impact only PO_4 and P_1 among the state variables.

When $u_{max,1}$ is halved, it leads to a higher PO_4 value compared to its default and double values, resulting in a negative percentage of variation. Doubling $K_{P,1}$ results in a higher PO_4 value compared to its default and halved values, leading to a positive percentage of variation.

Halving $g_{max,1}$ results in a higher P_1 value and a negative percentage of variation. Simultaneously, this leads to a lower PO_4 value compared to its default and halved values, resulting in a positive percentage of variation.

Doubling $K_{Z,1}$ results in a higher P_1 value and a positive percentage of variation. Conversely, halving $K_{Z,1}$ leads to a higher PO_4 value compared to its default and double values, causing a negative percentage of variation.

Fig. D.14 depicts the temporal evolution of eight parameters across three runs, with P_{supply} set to 0.10 $mmolC, m^{-3}d^{-1}$. Notably, changes in parameter values significantly influence the state variables, particularly P_2 and the R-ratio.

When $u_{max,1}$ is halved, it leads to a higher P_2 value compared to its default and double values. This results in a negative percentage of variation and a positive R-ratio percentage of variation. Similarly, halving $u_{max,2}$ results in a higher PO_4 value compared to its default and double values, causing a negative percentage of variation. Conversely, the percentage of variation of P_1 is negative, leading to a positive R-ratio percentage of variation.
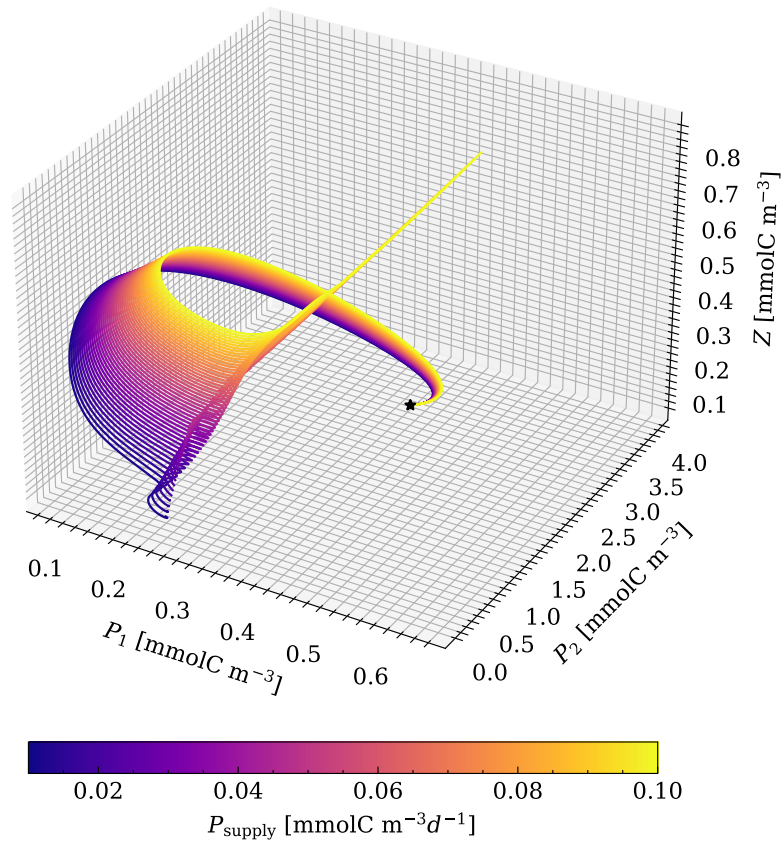
Figure C.12: Trajectories of plankton biomasses in a 3D phase space for a 2000-days simulation. The colour of each trajectory represents the parameter P_{supply} within the range of 50 values between 0.01 and 0.10. The black star represents the initial conditions, so this figure shows that, depending on P_{supply}, different equilibrium solutions are calculated.

Doubling $K_{P,1}$ leads to a higher P_2 value compared to its default and halved values, resulting in a positive percentage of variation and, consequently, a negative R-ratio percentage of variation. Conversely, halving $K_{P,2}$ results in a higher P_2 value compared to its default and double values, leading to a negative percentage of variation and, consequently, a positive R-ratio percentage of variation.

When $g_{max,1}$ is halved, it leads to a higher P_1 value and a negative percentage of variation. However, a lower P_2 value compared to its default and double values results in a positive percentage of variation and, consequently, a negative R-ratio percentage of variation.

Doubling $K_{Z,1}$ results in a higher P_1 value and a positive percentage of variation. Conversely, doubling $K_{Z,1}$ leads to a lower P_2 value compared to its default and halved values, causing a negative percentage of variation.

References

Acha, E.M., Piola, A., Iribarne, O., Mianzan, H., 2015. Ecological processes at marine fronts: oases in the ocean. Springer.

Adjou, M., Bendtsen, J., Richardson, K., 2012. Modeling the influence from ocean transport, mixing and grazing on phytoplankton diversity. Ecological modelling 225, 19–27. DOI:10.1016/j.ecolmodel.2011.11.005.

Auger, P.A., Diaz, F., Ulses, C., Estournel, C., Neveux, J., Joux, F., Pujo-Pay, M., Naudin, J., 2011. Functioning of the planktonic ecosystem on the gulf of lions shelf (NW Mediterranean) during spring and its impact on the carbon deposition: a field data and 3-d modelling combined approach. Biogeosciences 8, 3231–3261. DOI:10.5194/bg-8-3231-2011.

Aumont, O., Éthé, C., Tagliabue, A., Bopp, L., Gehlen, M., 2015. Pisces-v2: an ocean biogeochemical model for carbon and ecosystem studies. Geoscientific Model Development Discussions 8, 1375–1509. DOI:10.5194/gmdd-8-1375-2015.

Baklouti, M., Pagès, R., Alekseenko, E., Guyennon, A., Grégori, G., 2021. On the benefits of using cell quotas in addition to intracellular elemental ratios in flexible-stoichiometry plankton functional type models. application to the mediterranean sea. Progress in Oceanography 197, 102634. DOI:10.1016/j.pocean.2021.102634.
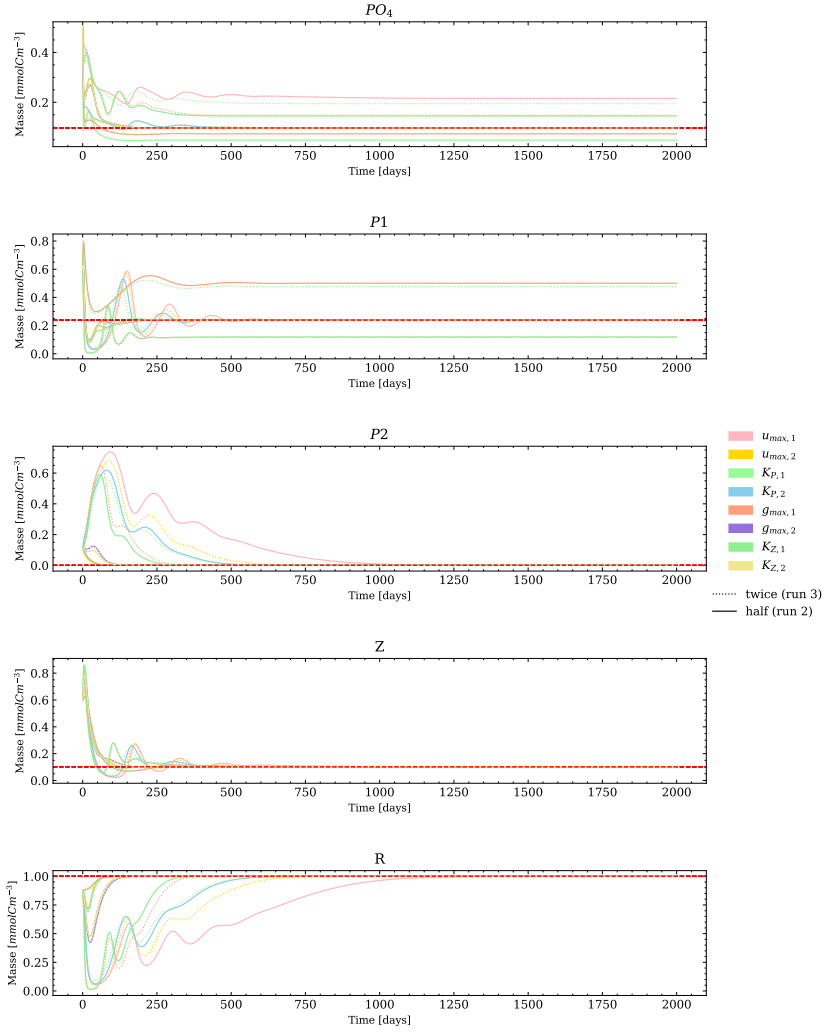
Figure D.13: Sensitivity test with P_{supply} equal to 0.01 $mmolC\,m^{-3}d^{-1}$. The different colours of the curves represent the parameters tested. Solid curves represent execution with half the default value (run 2), and dashed curves represent execution with twice the default value (run 3). The dotted red line represents the default value.

Figure D.14: Sensitivity test with P_{supply} equal to 0.10 $mmolC\,m^{-3}d^{-1}$. The different colours of the curves represent the parameters tested. Solid curves represent execution with half the default value (run 2), and dashed curves represent execution with twice the default value (run 3). The dotted red line represents the default value.
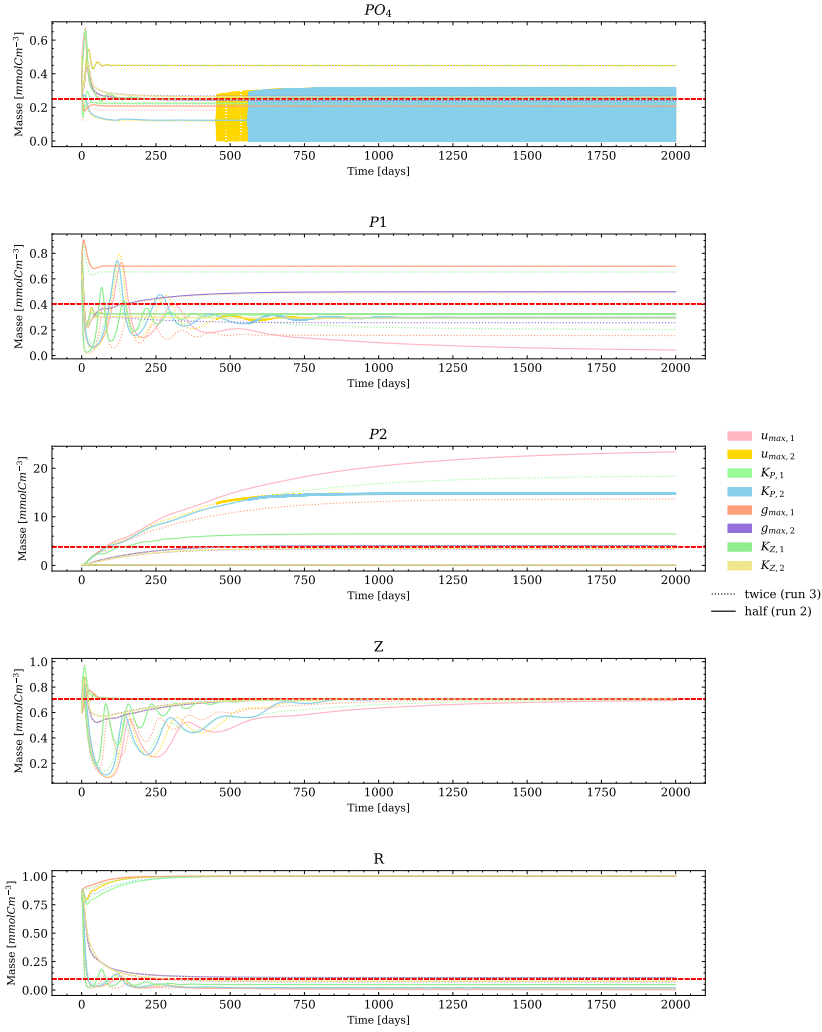
Behrenfeld, M.J., Boss, E.S., 2014. Resurrecting the ecological underpinnings of ocean plankton blooms. Annual review of marine science 6, 167–194. DOI:10.1146/annurev-marine-052913-021325.

Bohannan, B.J., Lenski, R.E., 2000. The relative importance of competition and predation varies with productivity in a model community. The American Naturalist 156, 329–340. DOI:10.1086/303393.

Clayton, S., Lin, Y.C., Follows, M.J., Worden, A.Z., 2017. Co-existence of distinct ostreococcus ecotypes at an oceanic front. Limnology and Oceanography 62, 75–88. DOI:10.1002/lno.10373.

Clayton, S., Nagai, T., Follows, M.J., 2014. Fine scale phytoplankton community structure across the kuroshio front. Journal of Plankton Research 36, 1017–1030. DOI:10.1093/plankt/fbu020.

Cunningham, A., Buonnacorsi, G.A., 1992. Narrow-angle forward light scattering from individual algal cells: implications for size and shape discrimination in flow cytometry. Journal of plankton research 14, 223–234. DOI:10.1093/plankt/14.2.223.

Doglioli, Gregori, 2023. Bioswot-med cruise, rv l'atalante. DOI:10.17600/18002392.

Droop, M.R., 1983. 25 years of algal growth kinetics a personal view DOI:10.1515/botm.1983.26.3.99.

Dumas, F., 2018. Protevsmed_swot_2018_leg1 cruise, rv beautemps-beaupré. DOI:10.17183/protevsmed-swot-2018-leg1.

Dutkiewicz, S., Cermeno, P., Jahn, O., Follows, M.J., Hickman, A.E., Taniguchi, D.A., Ward, B.A., 2020. Dimensions of marine phytoplankton diversity. Biogeosciences 17, 609–634. DOI:10.5194/bg-17-609-2020.

d'Ovidio, F., De Monte, S., Alvain, S., Dandonneau, Y., Lévy, M., 2010. Fluid dynamical niches of phytoplankton types. Proceedings of the National Academy of Sciences 107, 18366–18370. DOI:10.1073/pnas.1004620107.

Edwards, A.M., 2001. Adding detritus to a nutrient–phytoplankton–zooplankton model: a dynamical-systems approach. Journal of Plankton Research 23, 389–413. DOI:10.1093/plankt/23.4.389.

Foladori, P., Quaranta, A., Ziglio, G., 2008. Use of silica microspheres having refractive index similar to bacteria for conversion of flow cytometric forward light scatter into biovolume. Water research 42, 3757–3766. DOI:10.1016/j.watres.2008.06.026.

Franks, P.J., 2002. Npz models of plankton dynamics: their construction, coupling to physics, and application. Journal of Oceanography 58, 379–387. DOI:10.1023/A:1015874028196.

Frederiksen, M., Edwards, M., Richardson, A.J., Halliday, N.C., Wanless, S., 2006. From plankton to top predators: bottom-up control of a marine food web across four trophic levels. Journal of Animal Ecology 75, 1259–1268. DOI:10.1111/j.1365-2656.2006.01148.x.

Grant, S.R., 2014. Phosphorus uptake kinetics and growth of marine osmotrophs. Ph.D. thesis. [Honolulu]:[University of Hawaii at Manoa],[August 2014].

Grover, J.P., 1990. Resource competition in a variable environment: phytoplankton growing according to monod's model. The American Naturalist 136, 771–789. DOI:10.1086/285131.

Guieu, Desboeufs, 2017. Peacetime cruise, rv pourquoi pas? DOI:10.17600/17000300.

Hernández-Carrasco, I., Alou-Font, E., Dumont, P.A., Cabornero, A., Allen, J., Orfila, A., 2020. Lagrangian flow effects on phytoplankton abundance and composition along filament-like structures. Progress in Oceanography 189, 102469.

Hitchcock, G.L., Mariano, A.J., Rossby, T., 1993. Mesoscale pigment fields in the gulf stream: Observations in a meander crest and trough. Journal of Geophysical Research: Oceans 98, 8425–8445. DOI:10.1029/92JC02911.

Lévy, M., Ferrari, R., Franks, P.J., Martin, A.P., Rivière, P., 2012. Bringing physics to life at the submesoscale. Geophysical Research Letters 39. DOI:10.1029/2012gl052756.

Lévy, M., Franks, P.J., Smith, K.S., 2018. The role of submesoscale currents in structuring marine ecosystems. Nature communications 9, 4758. DOI:10.1038/s41467-018-07059-3.

Lévy, M., Jahn, O., Dutkiewicz, S., Follows, M.J., d'Ovidio, F., 2015. The dynamical landscape of marine phytoplankton diversity. Journal of The Royal Society Interface 12, 20150481. DOI:10.1098/rsif.2015.0481.

Lévy, M., Klein, P., Treguier, A.M., 2001. Impact of sub-mesoscale physics on production and subduction of phytoplankton in an oligotrophic regime 59, 535–565. DOI:10.1357/002224001762842181.

Longhurst, A., 1998. Ecological geography of the sea. academic press, san diego. 398 p .

Mahadevan, A., 2016. The impact of submesoscale physics on primary productivity of plankton. Annual review of marine science 8, 161–184. DOI:10.1146/annurev-marine-010814-015912.

Mahadevan, A., Archer, D., 2000. Modeling the impact of fronts and mesoscale circulation on the nutrient supply and biogeochemistry of the upper ocean. Journal of Geophysical Research: Oceans 105, 1209–1225. DOI:10.1029/1999JC900216.

Mangolte, I., 2022. Effet des fronts océaniques sur les communautés de plancton. Ph.D. thesis. Sorbonne Université.

Mangolte, I., Lévy, M., Dutkiewicz, S., Clayton, S., Jahn, O., 2022. Plankton community response to fronts: winners and losers. Journal of Plankton Research 44, 241–258. DOI:10.1093/plankt/fbac010.

Mangolte, I., Lévy, M., Haëck, C., Ohman, M.D., 2023. Sub-frontal niches of plankton communities driven by transport and trophic interactions at ocean fronts DOI:10.5194/egusphere-2023-471.

Marrec, P., Grégori, G., Doglioli, A.M., Dugenne, M., Della Penna, A., Bhairy, N., Cariou, T., Hélias Nunige, S., Lahbib, S., Rougier, G., et al., 2018. Coupling physics and biogeochemistry thanks to high-resolution observations of the phytoplankton community structure in the northwestern mediterranean sea. Biogeosciences 15, 1579–1606. DOI:10.5194/bg-15-1579-2018.

McCauley, E., Briand, F., 1979. Zooplankton grazing and phytoplankton species richness: Field tests of the predation hypothesis 1. Limnology and Oceanography 24, 243–252. DOI:10.4319/lo.1979.24.2.0243.

McWilliams, J.C., 2021. Oceanic frontogenesis. Annual Review of Marine Science 13, 227–253. DOI:10.1146/annurev-marine-032320-120725.

Menden-Deuer, S., Lessard, E.J., 2000. Carbon to volume relationships for dinoflagellates, diatoms, and other protist plankton. Limnology and oceanography 45, 569–579. DOI:10.4319/lo.2000.45.3.0569.

Messié, M., Chavez, F.P., 2017. Nutrient supply, surface currents, and plankton dynamics predict zooplankton hotspots in coastal upwelling systems. Geophysical Research Letters 44, 8979–8986. DOI:10.1002/2017GL074322.

Messié, M., Sancho-Gallegos, D.A., Fiechter, J., Santora, J.A., Chavez, F.P., 2022. Satellite-based lagrangian model reveals how upwelling and oceanic circulation shape krill hotspots in the california current system. Frontiers in Marine Science 9, 835813. DOI:10.3389/fmars.2022.835813.

Millot, C., Taupier-Letage, I., 2005. Circulation in the mediterranean sea. The Mediterranean Sea , 29–66DOI:10.1007/b107143.

Monod, J., 1942. Diauxie et respiration au cours de la croissance des cultures de b. coli, in: Annales de L'Institut Pasteur, Elsevier. pp. 548–550.

Moutin, T., Doglioli, A.M., De Verneil, A., Bonnet, S., 2017. Preface: The oligotrophy to the ultra-oligotrophy pacific experiment (outpace cruise, 18 february to 3 april 2015). Biogeosciences 14, 3207–3220.

Moutin, T., Raimbault, P., 2002. Primary production, carbon export and nutrients availability in western and eastern mediterranean sea in early summer 1996 (minos cruise). Journal of marine systems 33, 273–288. DOI:10.1016/S0924-7963(02)00062-3.

Munkes, B., Löptien, U., Dietze, H., 2021. Cyanobacteria blooms in the baltic sea: a review of models and facts. Biogeosciences 18, 2347–2378. DOI:10.5194/bg-18-2347-2021.

Peperzak, L., Zetsche, E.M., Gollasch, S., Artigas, L.F., Bonato, S., Créach, V., Vré, P.d., Dubelaar, G.B., Henneghien, J., Hess-Erga, O.K., et al., 2018. Comparing flow cytometry and microscopy in the quantification of vital aquatic organisms in ballast water, journal of marine engineering & technology DOI:10.1080/20464177.2018.1525806.

Poggiale, J.C., Eynaud, Y., Baklouti, M., 2013. Impact of periodic nutrient input rate on trophic chain properties. Ecological Complexity 14, 56–63. DOI:10.1016/j.ecocom.2013.01.005.

Polovina, J.J., Howell, E.A., Abecassis, M., 2008. Ocean's least productive waters are expanding. Geophysical Research Letters 35. DOI:10.1029/2007GL031745.

Prowe, A.F., Pahlow, M., Dutkiewicz, S., Follows, M., Oschlies, A., 2012. Top-down control of marine phytoplankton diversity in a global ecosystem model. Progress in Oceanography 101, 1–13. DOI:10.1016/j.pocean.2011.11.016.

Pulido-Villena, E., Desboeufs, K., Djaoudi, K., Van Wambeke, F., Barrillon, S., Doglioli, A., Petrenko, A., Taillandier, V., Fu, F., Gaillard, T., et al., 2021. Phosphorus cycling in the upper waters of the mediterranean sea (peacetime cruise): relative contribution of external and internal sources. Biogeosciences 18, 5871–5889. DOI:10.5194/bg-18-5871-2021.

Raick, C., Soetaert, K., Grégoire, M., 2006. Model complexity and performance: how far can we simplify? Progress in Oceanography 70, 27–57. DOI:10.1016/j.pocean.2006.03.001.

Sailley, S.F., Vogt, M., Doney, S.C., Aita, M.N., Bopp, L., Buitenhuis, E.T., Hashioka, T., Lima, I., Le Quéré, C., Yamanaka, Y., 2013. Comparing food web structures and dynamics across a suite of global marine ecosystem models. Ecological Modelling 261, 43–57. DOI:10.1016/j.ecolmodel.2013.04.006.

Taylor, A.G., Goericke, R., Landry, M.R., Selph, K.E., Wick, D.A., Roadman, M.J., 2012. Sharp gradients in phytoplankton community structure across a frontal zone in the california current ecosystem. Journal of Plankton Research 34, 778–789. DOI:10.1093/plankt/fbs036.

Thingstad, T.F., Rassoulzadegan, F., 1999. Conceptual models for the biogeochemical role of the photic zone microbial food web, with particular reference to the mediterranean sea. Progress in Oceanography 44, 271–286. DOI:10.1016/S0079-6611(99)00029-4.

Timmermans, K., Van der Wagt, B., Veldhuis, M., Maatman, A., De Baar, H., 2005. Physiological responses of three species of marine pico-phytoplankton to ammonium, phosphate, iron and light limitation. Journal of sea research 53, 109–120. DOI:10.1016/j.seares.2004.05.003.

Tzortzis, R., Doglioli, A.M., Barrillon, S., Petrenko, A.A., d'Ovidio, F., Izard, L., Thyssen, M., Pascual, A., Barceló-Llull, B., Cyr, F., et al., 2021. Impact of moderately energetic fine-scale dynamics on the phytoplankton community structure in the western mediterranean sea. Biogeosciences 18, 6455–6477. DOI:10.5194/bg-18-6455-2021.

Tzortzis, R., Doglioli, A.M., Barrillon, S., Petrenko, A.A., Izard, L., Zhao, Y., d'Ovidio, F., Dumas, F., Gregori, G., 2023. The contrasted phytoplankton dynamics across a frontal system in the southwestern mediterranean sea. Biogeosciences 20, 3491–3508. DOI:10.5194/bg-20-3491-2023.

Ward, B.A., Dutkiewicz, S., Follows, M.J., 2014. Modelling spatial and temporal patterns in size-structured marine plankton communities: top–down and bottom–up controls. Journal of Plankton Research 36, 31–47. DOI:10.1007/s00442-020-04768-9.

Yamamoto, T., Hatta, G., 2004. Pulsed nutrient supply as a factor inducing phytoplankton diversity. Ecological Modelling 171, 247–270. DOI:10.1016/j.ecolmodel.2003.08.011.

Yoder, J.A., McClain, C.R., Blanton, J.O., Oeymay, L.Y., 1987. Spatial scales in czcs-chlorophyll imagery of the southeastern us continental shelf 1 32, 929–941. DOI:10.4319/lo.1987.32.4.0929.

Zheng, Y., Gong, X., Gao, H., 2022. Selective grazing of zooplankton on phytoplankton defines rapid algal succession and blooms in oceans. Ecological Modelling 468, 109947.